Dalton Transactions

Variation of Electrocatalytic Activity of Isostructural Oxides Sr2LaFeMnO7 and Sr2LaCoMnO7 for Hydrogen and Oxygen-Evolution Reactions

Journal:	*Dalton Transactions*
Manuscript ID	DT-ART-06-2021-001977.R1
Article Type:	Paper
Date Submitted by the Author:	29-Aug-2021
Complete List of Authors:	Kananke-Gamage, Chandana ; University of Louisville Ramezanipour, Farshid; University of Louisville, Chemistry

Variation of Electrocatalytic Activity of Isostructural Oxides $Sr_2LaFeMnO_7$ and $Sr_2LaCoMnO_7$ for Hydrogen and Oxygen-Evolution Reactions

Chandana C.W. Kananke-Gamage[1], Farshid Ramezanipour[1,*]

[1]Department of Chemistry, University of Louisville, Louisville, KY 40292, USA

*Corresponding author. Email: farshid.ramezanipour@louisville.edu, Phone: +1(502) 852-7061

ORCID: 0000-0003-4176-1386

Abstract

The effect of the electronic configuration of transition metal on electrocatalytic activity, charge transport, and magnetic properties is demonstrated through investigation of $Sr_2LaFeMnO_7$ and $Sr_2LaCoMnO_7$. The two compounds are isostructural and contain bilayer stacks of octahedrally coordinated transition metals. Despite their structural similarity, the magnetic transition temperature of $Sr_2LaCoMnO_7$ is significantly lower than that of $Sr_2LaFeMnO_7$. The electrical charge-transport properties are also different, where $Sr_2LaCoMnO_7$ shows considerably improved electrical conductivity. Importantly, the electrocatalytic activities for the two half-reactions of water-splitting, i.e., hydrogen-evolution reaction (HER) and oxygen-evolution reaction (OER), are improved in $Sr_2LaCoMnO_7$ compared to $Sr_2LaFeMnO_7$. In addition, better kinetics for HER and OER are observed for $Sr_2LaCoMnO_7$, as evaluated by Tafel method. Furthermore, the electrochemically active surface area (ECSA) shows an enhancement for $Sr_2LaCoMnO_7$. Therefore, the trends in electrical charge transport, HER and OER activity, kinetic and ECSA are all similar, indicating the improved properties of $Sr_2LaCoMnO_7$. These changes are explained in the context of a greater bond covalency in this material due to the higher electronegativity of Co, which results in better overlap between the transition metal *d* orbital and oxygen *p* orbital. The relation between the electrocatalytic performance and the optimum eg orbital occupancy in $Sr_2LaCoMnO_7$ is also discussed.

1. Introduction

Oxide materials derived from perovskites have been studied for a wide range of applications, such as solar cells, batteries, catalysts, and capacitors.[1-4] One interesting family of perovskite-related oxides are the Ruddlesden-Popper materials, which have the general formula $A_{n+1}B_nO_{3n+1}$, where A is often a lanthanide or alkaline earth metal, and B is a transition metal. These materials contain perovskite-like connectivity, where BO_6 units share apexes to form layers that are stacked above each other. The number of layers in each stack is represented by *n* in the above formula. These materials have been investigated in different areas such as fuel cells,[5] photovoltaics[2] and photocatalysis.[2] For example, mixed ionic-electronic conducting Ruddlesden-Popper oxides have been examined as cathodes in solid oxide fuel cells, where the electrocatalytic activity toward the oxygen reduction reaction is needed.[5] These cathodes showed good cell performance at low-temperature, long-term stability, and chemical compatibility with a proton-conducting electrolyte.[5]

Also, a number of studies have focused on Ruddlesden-Popper oxides for electrocatalytic applications for water splitting.[6, 7] This is an important application given the need for efficient and economical electrocatalysts for the two half-reactions of water-splitting, namely hydrogen-evolution reaction (HER) and oxygen-evolution reaction (OER). The search for new electrocatalysts is essential, considering the high cost of traditional precious-metal catalysts, such as IrO_2 and RuO_2 for OER, and platinum is for HER. Various families of transition metal oxides have been studied for this purpose,[8, 9] and different parameters have been examined in search for design principles of effective catalysts.[7, 10, 11]

For Ruddlesden-Popper oxides, functional properties are often affected by changes to the A and B site metals, which change the electronic band structure. Correlations have been observed between the band gap of some Ruddlesden-Popper oxides and the ionic radii of B-site metals.[2] The

changes in transport and thermoelectric properties as a function of A and B site metals have also been demonstrated.[12]

Here, we investigate the effect of the B-site cation on electrocatalytic performance of two Ruddlesden-Popper materials, $Sr_2LaFeMnO_7$ and $Sr_2LaCoMnO_7$. Low temperature resistivity and magnetic measurements have been reported for these materials.[13-16] But electrocatalytic properties have not been investigated. Here we show that the variation in B-site cation can result in significant changes in the activity toward HER and OER processes. Furthermore, we have conducted electrical charge transport studies in a wide temperature-range and shown that the same trend is observed in both charge-transport and electrocatalytic properties as a function of B-site cation.

2. Experimental

2.1. Synthesis and Characterization

$Sr_2LaCoMnO_7$ and $Sr_2LaFeMnO_7$ were prepared by solid-state synthesis method. Stoichiometric amounts of $SrCO_3$, La_2O_3, MnO_2, Fe_2O_3 or CoO were mixed thoroughly using agate mortar and pestle, then pressed into pellets and heated at 1300 °C for 24 hours in air. The samples were then ground, re-pelletized and heated at 1300 °C in air for 72 hours with two intermittent grindings and pelletizing. The heating and cooling rates of the furnace for all samples were 100 °C/hour.

The synthesized materials were characterized by powder X-ray diffraction data using a high-resolution Cu Kα1 X-ray diffractometer (λ = 1.54056 Å). Rietveld refinements were carried out using GSAS softwar[17] and the EXPGUI interface.[18] The electrical conductivity measurements in air were done using two-probe DC technique on small cylindrical pellets by applying the potential of 0.01 V and collecting the output current. Magnetic susceptibility data were obtained in the temperature range of 2 K to 400 K with an applied magnetic field of 1000 Oe on a vibrating

sample magnetometer. Isothermal field-run measurements were also done in magnetic fields of 0 – 9 T. To examine the oxygen stoichiometry, iodometric titrations[19] were performed by dissolving 50 mg of the sample and excess KI (2 g) in 100 ml of 1 M HCl, which were left overnight to ensure the completion of the reaction. All steps were done under argon atmosphere. Then 5 ml of the solution was pipetted out and the iodine generated during the process was titrated against 0.025 M $Na_2S_2O_3$. A volume of 0.6 ml (12 drops) of starch solution was used as an indicator near the endpoint of the titration.

2.2. Electrocatalytic Measurements for OER and HER

The catalyst ink was prepared by mixing 35 mg of the Ruddlesden-Popper sample, 7 mg of carbon black powder (Fuel Cell Store), 40 μL Nafion® D-521 solution (Alfa Aesar, 5% w/w in water and 1-propanol) and 7 ml of THF (Alfa Aesar, 99%). After mixing, the solution mixture was sonicated for 30 minutes. This was followed by pipetting 20 μl of the catalyst ink and drop-casting it on the surface of a glassy carbon electrode (GCE), which served as working electrode. The drop-casting was done by placing two coats of 10 μl solution on GCE with a 2-minute interval. The GCE was then left overnight to air-dry before running the OER/HER measurements. Catalyst mass loading on GCE disk (diameter 5mm) was 0.1 mg. Prior to drop-casting, the GCE was furbished with aluminum oxide polishing solution (Allied Hightech Products Inc.) on a polishing cloth and sonicated for 2-3 minutes in ethanol (Decon Labs, Inc.). It was then washed with deionized water before use. The electrochemical OER/HER experiments were carried out in a standard three-electrode cell using an electrode rotator (Pine Research Instrumentation, Inc.) at 1600 rpm. A commercial Ag/AgCl in 1 M KCl (CH instruments, Inc., TX, USA) and a commercial Ag/AgCl in 4 M KCl (Pine Research Instrumentation, Inc.) were utilized as reference electrodes for OER and HER experiments respectively. A platinum electrode was used as the counter electrode in basic condition and a carbon electrode in acidic condition. Chronopotentiometry experiments under

HER conditions were done using this three electrode setup and a constant current of -1.9 mA. Also, chronopotentiometry experiments under OER conditions, with an applied current of 10 mA, were done using a two-electrode cell. Each electrode consisted of 1 cm^2 nickel foam, on which 100 µl of the catalyst ink had been dropcasted with 20 µl increments, followed by overnight air-drying. Gold wires were attached to the two electrodes, which had been separated by two layers of glass fiber filter paper. The two electrodes were soaked in 0.1M KOH for least 12 hours before performing the chronopotentiometry experiment. The potential versus silver/silver chloride ($E_{Ag/AgCl}$) was converted to be expressed against RHE using the equation $E_{RHE} = E_{Ag/AgCl} + 0.059\ pH + E^0_{Ag/AgCl}$, where $E^0_{Ag/AgCl} = 0.21$ V for 3M KCl[20] and 0.197 V for 4 M KCl.[21, 22]

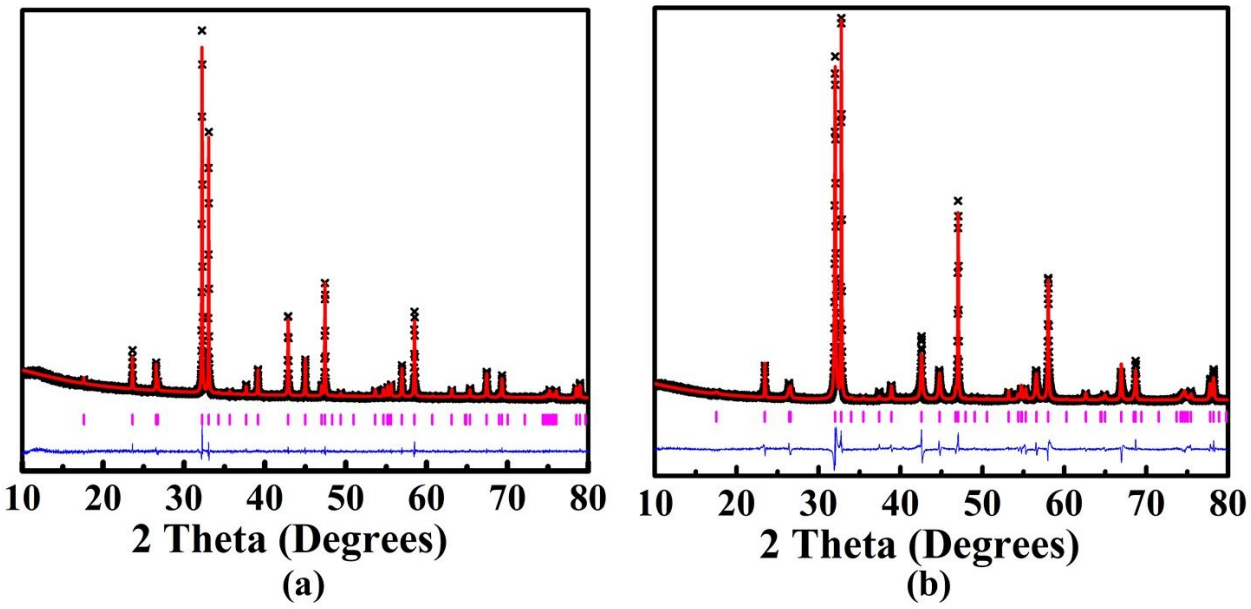

Figure 1. Rietveld refinement profiles for powder X-ray diffraction data for (a) $Sr_2LaCoMnO_7$ and (b)$Sr_2LaFeMnO_7$. The experimental data are represented by black crosses. The red line shows the fit. The vertical magenta tick marks, and the lower blue line correspond to the Bragg peak positions and difference plot, respectively.

3. Results and Discussion

3.1. Crystal Structure

The crystal structures of $Sr_2LaCoMnO_7$ and $Sr_2LaFeMnO_7$ were confirmed by Rietveld refinements using powder X-ray diffraction data. The Rietveld refinement profiles for the two compounds are shown in Figure 1. Both materials crystalize in tetragonal *I*4/*mmm* space group, consistent with previous structural reports.[13,16] The refined structural parameters are listed in Tables 1 and 2.

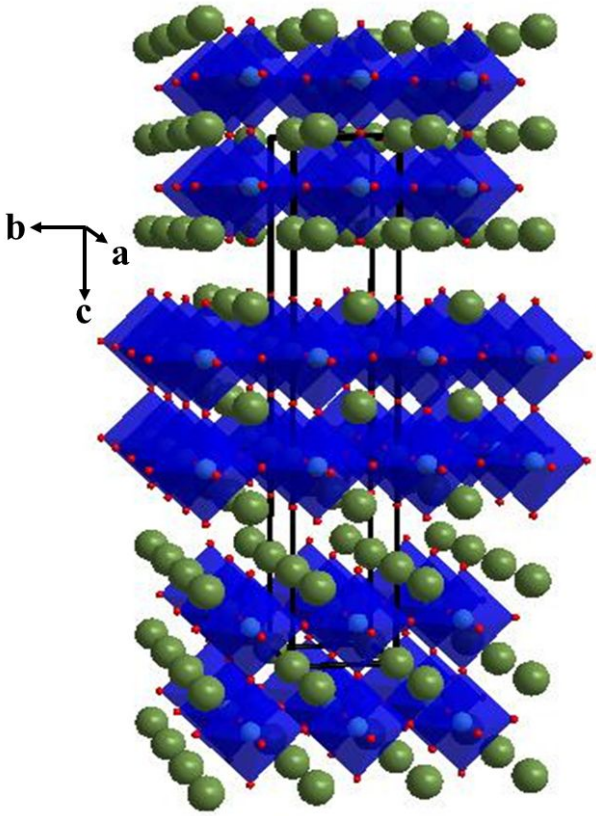

Figure 2. Crystal structure of $Sr_2LaBMnO_7$ (B = Fe, Co). Green spheres represent Sr/La, and red spheres show oxygens. The BO_6 octahedra are shown in dark blue.

The crystal structure of these Ruddlesden-Popper oxides, $A_{n+1}B_nO_{3n+1}$ (n = 2), consists of bilayer stacks of BO_6 octahedra. As shown in Figure 2, the BO_6 units (B = Mn, Fe or Co) form a two-

dimensional network by sharing the corner oxygens. Each octahedron shares one of its apical oxygens and all four of its equatorial oxygens with other octaherda.[23] The spaces between the BO_6 octahedra are occupied by the A-site cations. Therefore, there are two crystallographically distinct positions for A-site cations, one within and another between the octahedral stacks. Thus, the formula can be represented as $AA'_2B_2O_7$,[23] where A and A' indicate the metals located in intra and inter-stack spaces, respectively.

Table 1: Refined structural parameters of $Sr_2LaCoMnO_7$ from powder X-ray diffraction data.

Atom	x	y	z	Occupancy	U_{iso} (Å^2)	Multiplicity
Sr1	0	0	0.18233(9)	0.6667	0.034(1)	4
La1	0	0	0.18233(9)	0.3333	0.034(1)	4
Sr2	0	0	0	0.6667	0.010(1)	2
La2	0	0	0	0.3333	0.010(1)	2
Mn	0	0	0.4020(2)	0.5	0.024(1)	4
Co	0	0	0.4020(2)	0.5	0.024(1)	4
O1	0	0	0.5	1	0.036(9)	2
O2	0	0	0.3039(7)	1	0.040(6)	4
O3	0	0.5	0.0945(6)	1	0.028(3)	8

Space group: I4/mmm, $a = b = 3.83116(5)$ Å, $c = 20.1327(3)$ Å, Rp = 0.0359, wRp = 0.0446

Table 2: Refined structural parameters of $Sr_2LaFeMnO_7$ from powder X-ray diffraction data.

Atom	x	y	z	Occupancy	U_{iso} (Å^2)	Multiplicity
Sr1	0	0	0.5	0.6667	0.027(2)	2
La1	0	0	0.5	0.3333	0.027(2)	2
Sr2	0	0	0.3166(1)	0.6667	0.047(2)	4
La2	0	0	0.3166(1)	0.3333	0.047(2)	4
Mn	0	0	0.1004(3)	0.5	0.016(1)	4
Fe	0	0	0.1004(3)	0.5	0.016(1)	4
O1	0	0	0	1	0.043(2)	2
O2	0	0	0.1899(8)	1	0.043(2)	4
O3	0	0.5	0.0928(9)	1	0.043(2)	8

Space group: I4/mmm, $a = b = 3.8617(1)$ Å, $c = 20.2300(6)$ Å, Rp = 0.0360, wRp = 0.0558

While the structures of $Sr_2LaFeMnO_7$ and $Sr_2LaCoMnO_7$ are similar, the two compounds show slightly different unit volumes, i.e., 301.68(2) $Å^3$ and 295.50(1) $Å^3$, respectively. This is consistent with the difference in the ionic radii of Fe^{3+} and Co^{3+}, which are 0.645 Å and 0.61 Å, respectively.[24] To examine the oxygen contents of these materials, iodometric titrations were done, which indicated 7 oxygens per formula unit for both compounds. Scanning electron microscopy was used to evaluate the microstructure of the compounds. As shown in Figure 3, these data indicate larger grain size for $Sr_2LaCoMnO_7$ compared to $Sr_2LaFeMnO_7$.

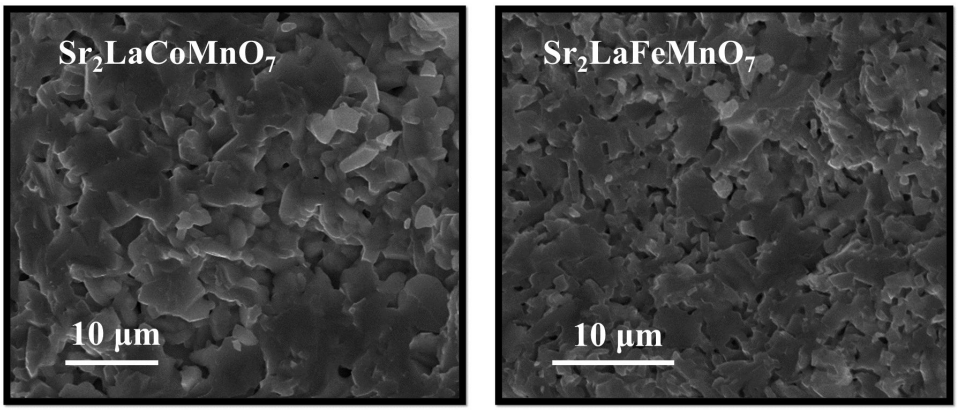

Figure 3. Scanning electron microscopy images for $Sr_2LaCoMnO_7$ compared to $Sr_2LaFeMnO_7$.

3.2. Electrical Conductivity

The electrical properties of these materials were investigated in the temperature range 25 – 800 ^oC, indicating the effect of the change in the B-site cation. Electrical conductivity was obtained from the measured resistance (R) using the following equation:

$$\sigma = L/RA \qquad (1)$$

Here, σ is the conductivity, L is the thickness of the measured pellet, and A is the cross-sectional area of the pellet. The variation of electrical conductivity as a function of temperature is

illustrated in Figure 4a. As observed in this figure, $Sr_2LaCoMnO_7$ shows significantly greater conductivity than $Sr_2LaFeMnO_7$ in the entire temperature range.

Both compounds show an increase in electrical conductivity as temperature increases beyond room temperature, but the conductivity of $Sr_2LaCoMnO_7$ plateaus and then decreases when the temperature is raised above 500 °C. The activation energy[25] can be found using the Arrhenius equation for thermally activated increase in conductivity:[26, 27]

$$\sigma T = \sigma_0 e^{-\frac{E_a}{k_B T}} \quad (2)$$

Here, σ, σ_0, T, E_a, and k_B represent conductivity, pre-exponential factor, temperature, activation energy, and the Boltzmann constant, respectively. The Arrhenius plots for $Sr_2LaFeMnO_7$ and $Sr_2LaCoMnO_7$ are shown in Figure 4b. It is noted that the activation energy here represents the energy barrier for the temperature-dependent increase in conductivity.

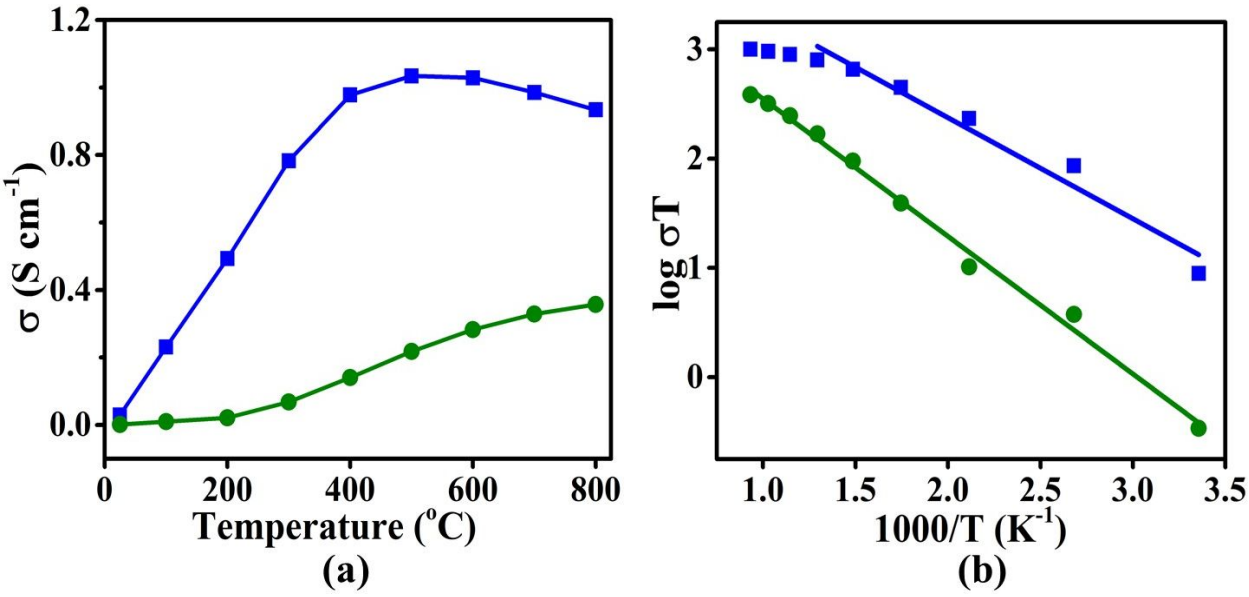

Figure 4. (a) Electrical conductivity variation as a function of temperature for $Sr_2LaFeMnO_7$ (green) and $Sr_2LaCoMnO_7$ (blue). **(b)** Arrhenius plots for determination of the activation energies (E_a) for the temperature-activated increase in conductivity, giving E_a = 0.2499 (25-800 °C) for $Sr_2LaMnCoO_7$ and E_a = 0.194 (25-500 °C) for $Sr_2LaMnCoO_7$.

The electrical conduction in oxide materials often occurs through the B–O–B pathways, where B is usually a transition metal with hetero-valency. The overlap of the 3d orbitals of the transition metal with the 2p orbitals of oxygen allows the electron conduction. This overlap can be enhanced by shorter B–O bonds and larger B–O–B angles, i.e., angles closer to 180°.[27] While the average B–O bond distance is similar for both compounds, the average B–O–B bond angle for $Sr_2LaCoMnO_7$, 177.9(5)°, is greater than that of $Sr_2LaFeMnO_7$, 175.5(8)°.

3.3. Magnetic Properties

The change in the B-site cation results in significant changes in magnetic properties. Figures 5a and 5b illustrate the magnetic susceptibility (χ) of $Sr_2LaCoMnO_7$ and $Sr_2LaFeMnO_7$ in the temperature range 2 K – 400 K. The magnetic susceptibility data for $Sr_2LaCoMnO_7$ indicate a transition at ~85 K and splitting of the zero-field-cooled (ZFC) and field-cooled (FC) data below ~70 K. This is similar to the behavior that was previously reported for this material and was attributed to a spin-glass transition.[15, 16] The spin-glass state was explained in terms of competing ferromagnetic (Mn^{4+}–Co^{3+}) and antiferromagnetic (Mn^{4+}–Mn^{4+} and Co^{3+}–Co^{3+}) superexchange interactions.[16]

To determine the effect of the change in B-site cation, we also obtained magnetic susceptibility data for $Sr_2LaFeMnO_7$, which showed a similar behavior to the Co-analogue, but with a less pronounced transition occurring at ~150 K. Similar to the Co-analogue discussed above, competing ferromagnetic (Mn^{4+}–Fe^{3+}) and antiferromagnetic (Mn^{4+}–Mn^{4+} and Fe^{3+}–Fe^{3+}) superexchange couplings are expected. The greater magnetic moment of Fe^{3+} compared with Co^{3+} is likely the reason for the observation of the magnetic transition at a higher temperature for $Sr_2LaFeMnO_7$ than $Sr_2LaCoMnO_7$.

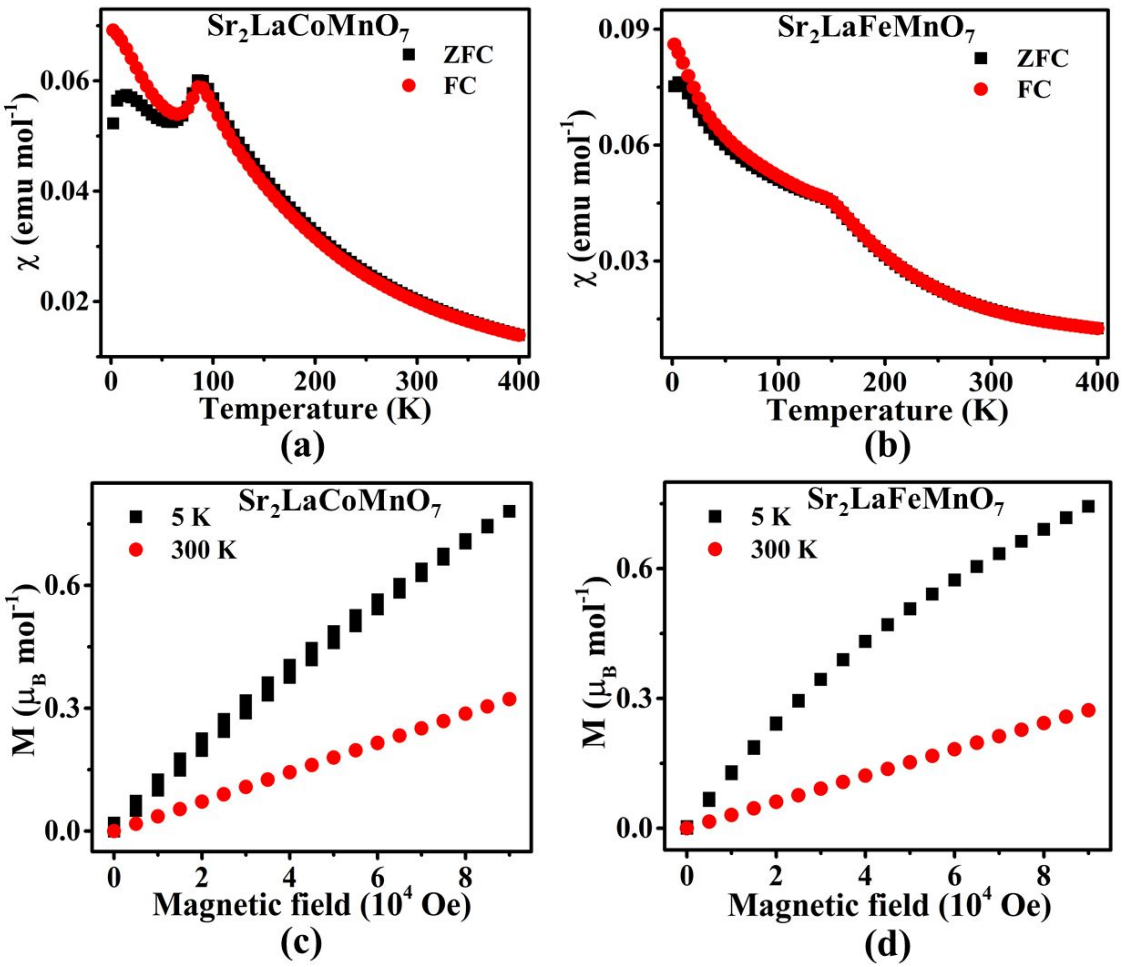

Figure 5. **(a)** and **(b)** show zero-field-cooled (ZFC) and field-cooled (FC) magnetic susceptibility data. (**c**) and (**d**) show the isothermal magnetization data as a function of magnetic field.

The isothermal field sweep data were obtained for both compounds at 5 K and 300 K, as shown in Figures 5c and 5d. The data at 300 K are linear for both materials, as expected for a paramagnetic state. However, at 5 K, deviations from linear behavior are observed for both compounds, with $Sr_2LaMnCoO_7$ showing small hysteresis, indicating the presence of uncompensated moments at low temperature.

Overall, the main effect of the change in the B-site cation is the shift in the magnetic transition temperature from ~85 K for $Sr_2LaCoMnO_7$ to ~150 K in $Sr_2LaFeMnO_7$.

3.4. Electrocatalytic Activity for HER

The change in the B-site cation has a major impact on the electrocatalytic activity toward both hydrogen-evolution reaction (HER) and oxygen-evolution reaction (OER). The broadly accepted mechanism for HER starts with Volmer reaction, followed by either Heyrovsky or Tafel reaction.[28, 29]

Volmer (acidic): $H_3O^+ + M + e^- \rightleftharpoons M–H^* + H_2O$
Volmer (alkaline): $H_2O + M + e^- \rightleftharpoons M–H^* + OH^-$
Heyrovsky (acidic): $M–H^* + H_3O^+ + e^- \rightleftharpoons M + H_2 + H_2O$
Heyrovsky (alkaline): $M–H^* + H_2O + e^- \rightleftharpoons M + H_2 + OH^-$
Tafel (or acidic alkaline): $2M–H^* \rightleftharpoons 2M + H_2$

In this work, the HER experiments were initially performed in typical alkaline conditions (1 M KOH),[30, 31] showing little electrocatalytic activity. Therefore, the acidic conditions, 0.1 M $HClO_4$ and 0.5 M H_2SO_4, which are common in HER experiments,[32, 33] were evaluated. While 0.1 M $HClO_4$ led to low HER activity, better performance was observed in 0.5 M H_2SO_4. As shown in Figure 6a, under this condition, $Sr_2LaCoMnO_7$ shows considerably better electrocatalytic properties for HER than $Sr_2LaFeMnO_7$. The HER overpotential at 10 mA/cm^2, η_{10}, is -693 mV for the latter and -612 mV for the former, which also shows a greater current response. In addition, HER data using Pt/C catalyst was also obtained as a reference, giving overpotential of $\eta_{10} \approx 20$ mV consistent with previous reports.[34, 35] The HER activities of $Sr_2LaFeMnO_7$ and $Sr_2LaCoMnO_7$ are not as high as those observed for Pt/C[34, 35] or some oxide catalysts such as $SrCa_2GaMn_2O_8$ (η_{10} = -315 mV).[30] However, the activity of $Sr_2LaCoMnO_7$ is better than that of some other oxide electrocatalysts such as TiO_{2-x} (η_{10} = -630 mV)[36] and WO_3 (η_{10} = -637 mV).[37] The reaction kinetics was evaluated using Tafel equation,[38] $\eta = a + b \log j$, where η is the overpotential and j is the current density. The slope of the Tafel plot, η vs log j, is affected by electron and mass transport. Smaller

Tafel slopes indicate faster reaction kinetics. As shown in Figure 6b, the Tafel slopes are 239 mV/dec and 141 mV/dec for $Sr_2LaFeMnO_7$ and $Sr_2LaCoMnO_7$, respectively. This is consistent with greater electrocatalytic activity of $Sr_2LaCoMnO_7$, which also shows a stable response in chronopotentiometry data for 12 hours, as shown in Figure 6c.

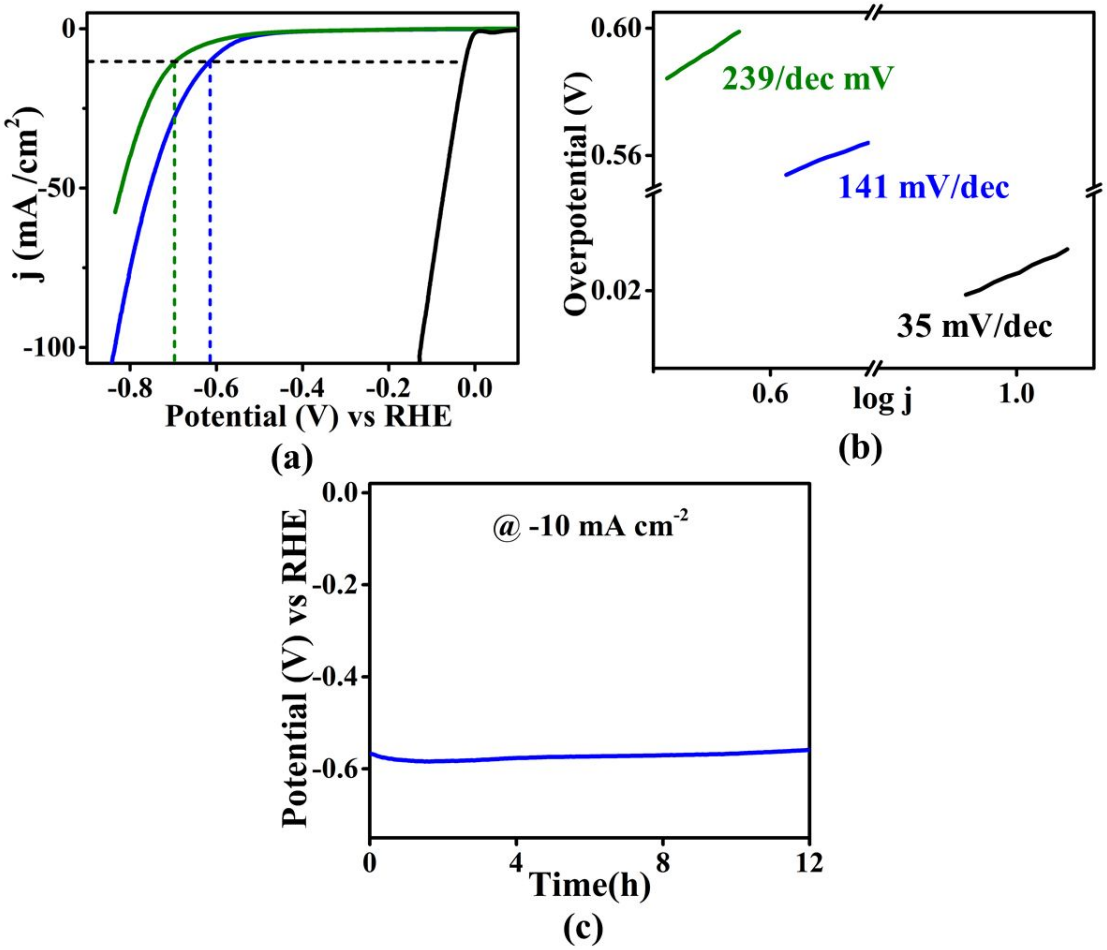

Figure 6. HER activity in 0.5 M H_2SO_4 for $Sr_2LaFeMnO_7$ (green), $Sr_2LaCoMnO_7$ (blue), and Pt/C (black): **(a)** Polarization curves. **(b)** Tafel plots. **(c)** Chronopotentiometry for $Sr_2LaCoMnO_7$.

3.5. Electrocatalytic Activity for OER

The OER in alkaline environment has been described as a multi-step process, as shown below:[29, 39]

$$M + OH^- \rightleftharpoons M\text{-}OH + e^-$$
$$M\text{-}OH + OH^- \rightleftharpoons M\text{-}O + H_2O + e^-$$
$$M\text{-}O + OH^- \rightleftharpoons M\text{-}OOH + e^-$$

$$M\text{-}OOH + OH^- \rightleftharpoons M + O_2 + H_2O + e^-$$

Similarly the OER mechanism in acidic condition has been described as follows:[29, 39]

$$M + H_2O \rightleftharpoons M\text{-}OH + H^+ + e^-$$
$$M\text{-}OH \rightleftharpoons M\text{-}O + H^+ + e^-$$
$$M\text{-}O + H_2O \rightleftharpoons M\text{-}OOH + H^+ + e^-$$
$$M\text{-}OOH \rightleftharpoons M + O_2 + H^+ + e^-$$

Figure 7a shows polarization curves for the OER activity of both $Sr_2LaFeMnO_7$ and $Sr_2LaCoMnO_7$ in a typical OER electrolyte, 0.1 M KOH. As evident from these data, the change in B-site metal results in a significant improvement in the OER activity. The OER overpotential, η_{10}, beyond the ideal potential of 1.23 V, is evaluated at 10 mA/cm^2. The polarization curve for $Sr_2LaFeMnO_7$ does not even reach 10 mA/cm^2, indicating the low OER activity of this compound. On the other hand, $Sr_2LaCoMnO_7$ shows overpotential of η_{10} = 538 mV. In addition, OER data using IrO_2 catalyst was also obtained as a reference, giving overpotential of $\eta_{10} \approx$ 400 mV, consistent with previous reports.[40, 41] The OER activities of $Sr_2LaFeMnO_7$ and $Sr_2LaCoMnO_7$ are not as high as those observed for some oxides such as IrO_2,[40, 41] RuO_2 ($\eta_{10} \approx$ 420 mV)[42] and $CaSrFeMnO_{6-\delta}$ (η_{10} = 370 mV).[33] However, the activity of $Sr_2LaCoMnO_7$ is close to that of the well-known oxide catalyst BSCF ($\eta_{10} \approx$ 500 mV).[41] In addition, its activity is superior to some other reported OER electrocatalysts, such as $La_{0.5}Sr_{0.5}Co_{0.8}Fe_{0.2}O_3$ (η_{10} = 600 mV)[43], $La_{0.6}Sr_{0.4}CoO_{3-\delta}$ (η_{10} = 590 mV)[44], and $La_{0.5}Sr_{0.5}CoO_{3-\delta}$ (η_{10} = 600 mV).[45]

The significant difference in the catalytic activity is also evident from the OER kinetics, evaluated using the Tafel plot in Figure 7b. The Tafel slope for $Sr_2LaCoMnO_7$ is 123 mV/dec as compared to 151 mV/dec for $Sr_2LaFeMnO_7$. In addition, chronopotentiometry data for $Sr_2LaCoMnO_7$ show a stable response for 12 hours, as shown in Figure 7c.

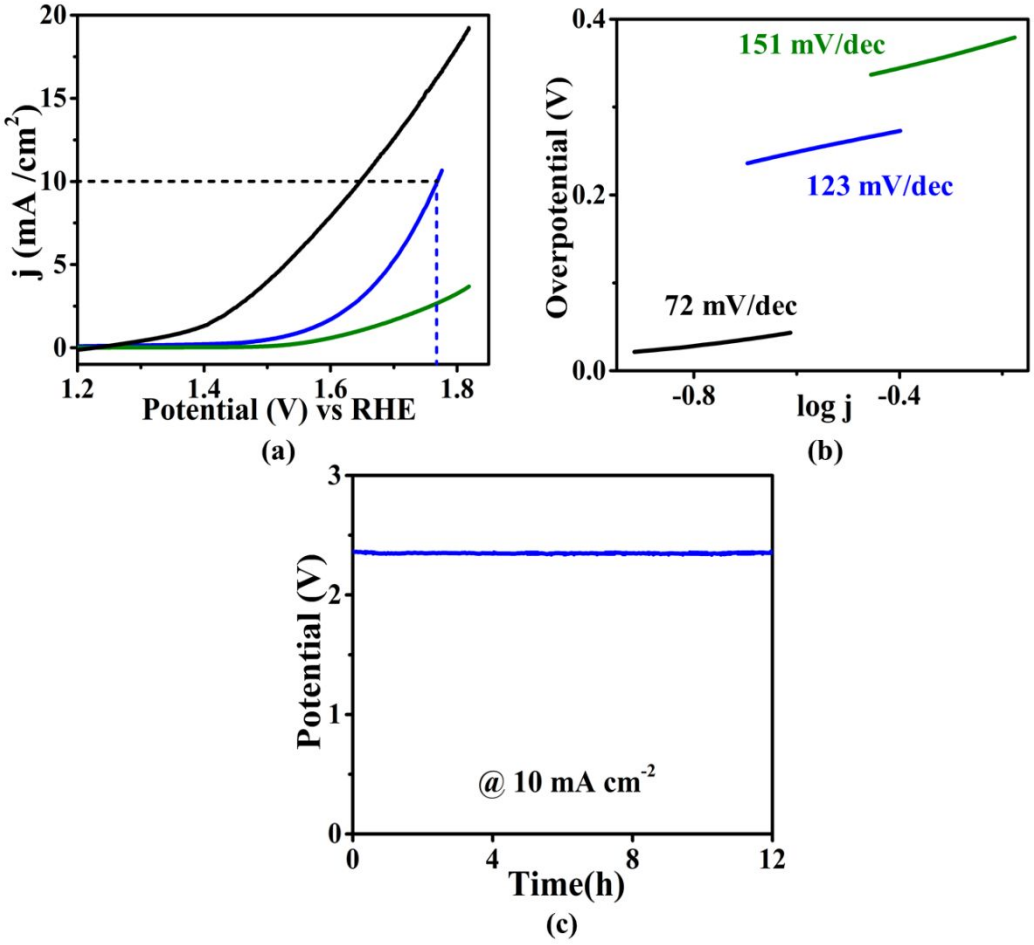

Figure 7. OER activity in 0.1 M KOH for $Sr_2LaFeMnO_7$ (green), $Sr_2LaCoMnO_7$ (blue), and IrO_2 (black): **(a)** Polarization curves. **(b)** Tafel plots. **(c)** Chronopotentiometry response of $Sr_2LaCoMnO_7$.

Furthermore, the electrochemically active surface areas (ECSA) were evaluated for the two materials. The ECSA is related to double-layer capacitance (C_{dl}) through the equation $ECSA=C_{dl}/C_s$, where C_s is specific capacitance. Given the direct relationship between ECSA and C_{dl}, it is common to use the value of C_{dl} as an indication of the magnitude of ECSA.[46, 47] The double layer capacitance is obtained using cyclic voltammetry data in the non-Faradaic region (Figure 8a and b), where the electrode reactions are insignificant and the current originates from electrical double layer charge and discharge. The C_{dl} is evaluated using the relationship C_{dl} =

$j_{average}/\nu$, where ν is the scan rate and $j_{average}$ is the average of the absolute values of j_{anodic} and $j_{cathodic}$ from cyclic voltammetry.[46] Therefore, the value of C_{dl} is obtained using the slope of the plot of $j_{average}$ versus ν. As shown in Figure 8c, $Sr_2LaCoMnO_7$ has a significantly greater C_{dl}, which is consistent with the higher electrocatalytic activity of this material compared with $Sr_2LaFeMnO_7$. X-ray diffraction data before and after 1000 cycles of OER showed a small shift of diffraction peaks to the right, but indicated the retention of the structural integrity of $Sr_2LaCoMnO_7$ upon its application as an electrocatalyst, as shown in Figure 9.

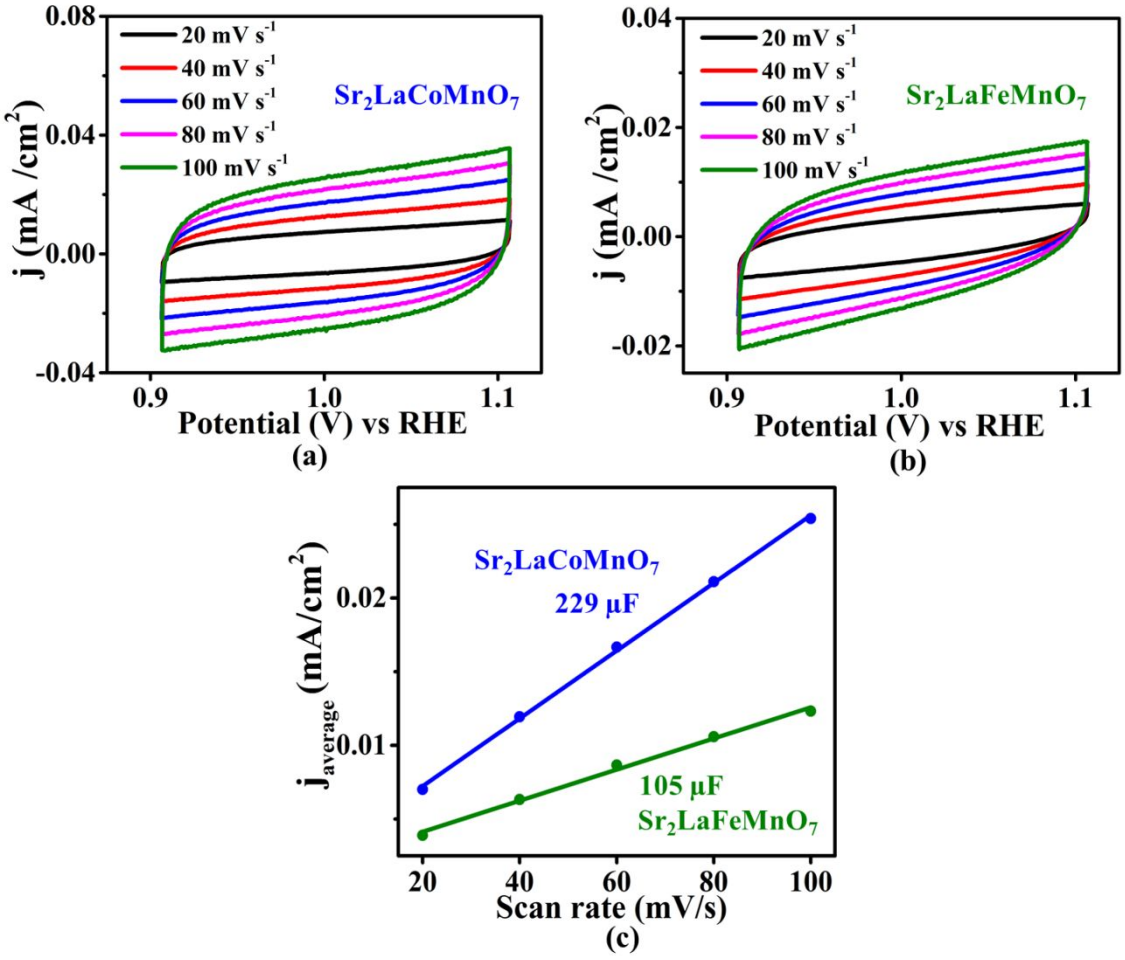

Figure 8. (a) and (b) cyclic voltammetry in non-Faradaic region in 0.1 M KOH. (c) $j_{average}$ obtained from these CV plotted as a function of scan rate. The slope gives double layer capacitance.

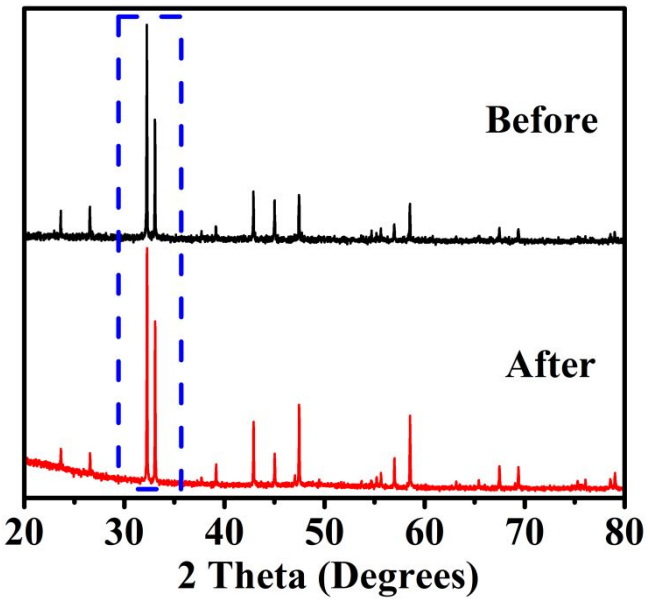

Figure 9. X-ray diffraction data for $Sr_2LaCoMnO_7$ before and after 1000 cycles of OER.

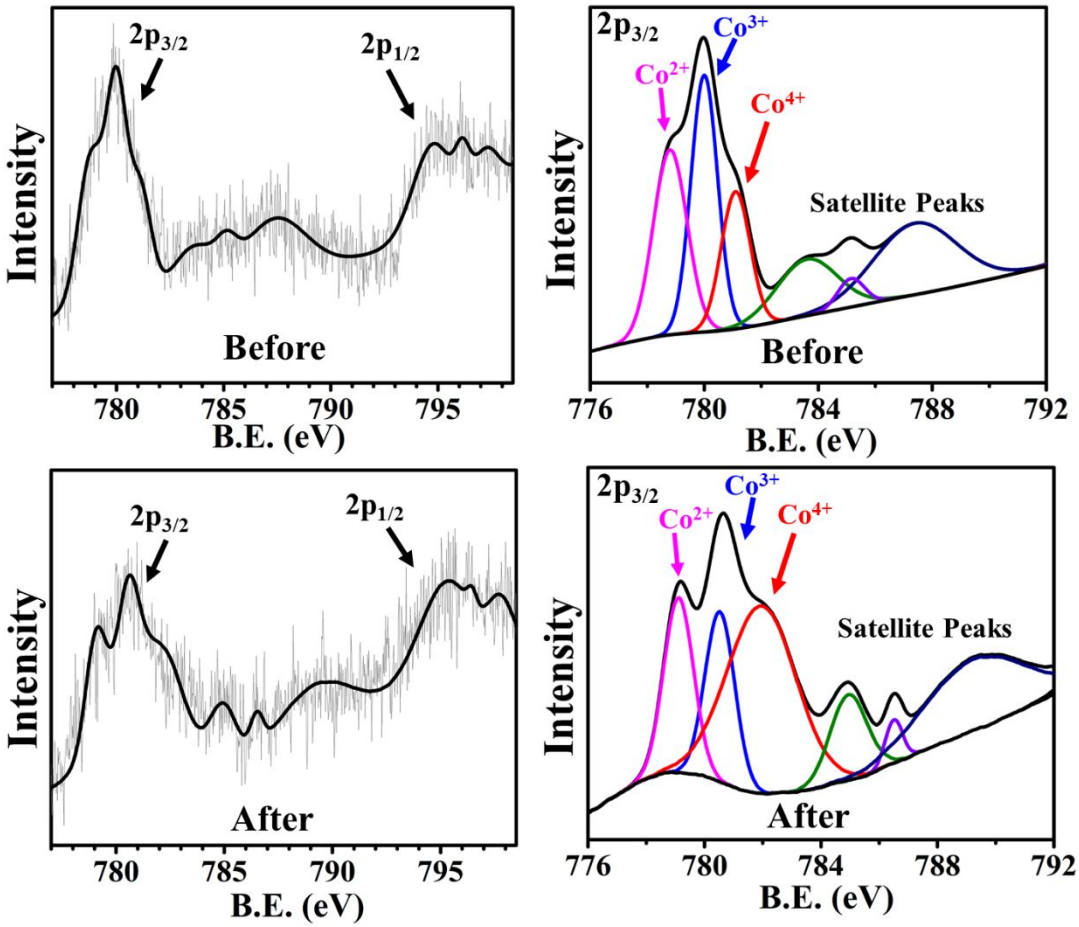

Figure 10. X-ray photoelectron spectroscopy data, showing cobalt binding energies, for $Sr_2LaCoMnO_7$ before (top) and after (bottom) 1000 cycles of OER.

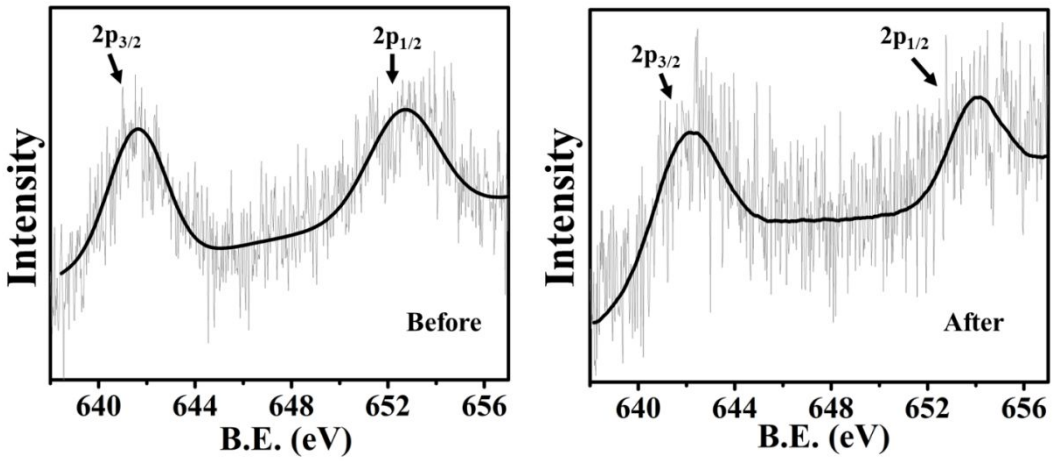

Figure 11. X-ray photoelectron spectroscopy data, showing manganese binding energies, for $Sr_2LaCoMnO_7$ before and after 1000 cycles of OER.

In addition, X-ray photoelectron spectroscopy data for $Sr_2LaCoMnO_7$ before and after 1000 cycles of OER (Figures 10 and 11), indicated a small shift of the binding energies to the right, which could indicate a small increase in the average oxidation states of metal, but the material retains the same types of metal oxidation states, as shown in Figures 10 and 11.

The enhanced electrocatalytic properties of $Sr_2LaCoMnO_7$ over $Sr_2LaFeMnO_7$ can be explained in terms of greater electronegativity of Co compared to Fe, which leads to a decrease in metal-to-ligand charge-transfer energy[48, 49] as well as a higher degree of covalency for the bonds between the transition metal and oxygen.[10] The improved covalency has been shown to positively impact the electrocatalytic activity, particularly for OER, where better overlap between metal d and oxygen p orbital is acheived.[10]

Another parameter that has been shown to correlate with the electrocatalytic activity of some oxide materials is the electron occupancy of the e_g orbitals, which affects the strength of sigma bonding between the catalyst and reaction intermediates.[50] It has been suggested that e_g orbital occupancy of ~1 is optimum for achieving enhanced electrocatalytic properties.[51] The two compounds

$Sr_2LaFeMnO_7$ and $Sr_2LaCoMnO_7$ contain Fe^{3+} and Co^{3+}, respectively. Trivalent Fe is often in high spin state in perovskite-related oxides, giving t_{2g}^3 e_g^2. However, previous studies have shown intermediate spin for Co^{3+} in perovskite-related oxides,[51, 52] which gives t_{2g}^5 e_g^1, where the eg orbital occupancy is 1. This could be another parameter that explains the higher electrocatalytic activity of $Sr_2LaCoMnO_7$.

Conclusions

Functional properties of Ruddlesden-Popper oxides can be changed by varying the B-site cation. We have shown that magnetic transition temperature can be shifted significantly by changing the B-site cation from Fe^{3+} to Co^{3+}. In addition, charge transport properties can be enhanced. $Sr_2LaCoMnO_7$ shows considerably greater electrical conductivity than $Sr_2LaFeMnO_7$. Furthermore, the change in the B-site cation helps to improve the electrocatalytic activity toward hydrogen-evolution reaction (HER) and oxygen-evolution reactions (OER). $Sr_2LaCoMnO_7$ shows significantly enhanced catalytic activity for both HER and OER, as well as better reaction kinetics and electrochemically active surface area. These changes are assigned to the higher electronegativity of Co compared to Fe, resulting in greater bond covalency and better overlap of metal-oxygen orbitals. In addition, the electronic configuration and the eg orbital occupancy may play a role in the improvement of electrocatalytic properties in $Sr_2LaCoMnO_7$ as compared to $Sr_2LaFeMnO_7$.

Conflicts of interest

The authors declare no conflict of interest.

Acknowledgements

This work is supported in part by the National Science Foundation under Grant No. DMR-1943085.

References

1. A. C. Tomkiewicz, M. Tamimi, A. Huq and S. McIntosh, *J. Mater. Chem. A*, 2015, **3**, 21864-21874.
2. A. Chen, X. Zhang, Z. Zhang, S. Yao and Z. Zhou, *J. Mater. Chem. A*, 2019, **7**, 11530-11536.
3. J. T. Mefford, W. G. Hardin, S. Dai, K. P. Johnston and K. J. Stevenson, *Nat. Mater*, 2014, **13**, 726-732.
4. M. S. Alom and F. Ramezanipour, *Mater. Lett.*, 2021, **295**, 129859.
5. Q. Wang, J. Hou, Y. Fan, X.-a. Xi, J. Li, Y. Lu, G. Huo, L. Shao, X.-Z. Fu and J.-L. Luo, *J. Mater. Chem. A* . 2020, **8**, 7704-7712.
6. Y. Zhu, H. A. Tahini, Z. Hu, J. Dai, Y. Chen, H. Sun, W. Zhou, M. Liu, S. C. Smith, H. Wang and Z. Shao, *Nat. Commun.*, 2019, **10**, 149.
7. M. Ebrahimizadeh Abrishami, M. Risch, J. Scholz, V. Roddatis, N. Osterthun and C. Jooss, *Materials (Basel)*, 2016, **9**, 921.
8. A. Vojvodic and J. Nørskov, *Science (New York, N.Y.)*, 2011, **334**, 1355-1356.
9. Y. Matsumoto and E. Sato, *Mater. Chem. Phys.*, 1986, **14**, 397-426.
10. J. Suntivich, W. T. Hong, Y.-L. Lee, J. M. Rondinelli, W. Yang, J. B. Goodenough, B. Dabrowski, J. W. Freeland and Y. Shao-Horn, *J. Phys. Chem. C*, 2014, **118**, 1856-1863.
11. R. K. Hona and F. Ramezanipour, *Inorg. Chem.*, 2020, **59**, 4685-4692.
12. R. Sun, X.-y. Qin, L. L. Li, D.-D. Li, J. Zhang and Q. Wang, *J. Phys. D: Appl. Phys*, 2012, **45**, 415401.
13. I. B. Sharma, S. K. Magotra, D. Singh, S. Batra and K. D. S. Mudher, *J. Alloys Compd.* , 1999, **291**, 16-20.
14. D. Singh, S. Sharma, A. Mahajan, Singh and R. Singh, *Ionics*, 2013, **19**, 1603–1610.
15. T. I. Chupakhina and G. V. Bazuev, *Russ. J. Inorg*, 2008, **53**, 681-685.
16. H. El-Shinawi, A. Bertha, J. Hadermann, T. Herranz, J. Marco, F. Berry and C. Greaves, *J. Solid State Chem.*, 2010, **183**, 1347–1353.
17. A. C. L. a. R. B. V. Dreele, *Los Alamos National Laboratory Report LAUR*, 2004, 86–748.
18. B. H. Toby, *J. Appl. Crystallogr.*, 2001, **34**, 210-213.
19. R. K. Hona and F. Ramezanipour, *J. Mater. Sci.: Mater. Electron.*, 2018, **29**, 13464-13473.
20. K. M. Jeerage, S. L. Candelaria and S. M. Stavis, *Sci. Rep.*, 2018, **8**, 4584.
21. X. Du, G. Ma and X. Zhang, *ACS Sustain. Chem. Eng.*, 2019, **7**, 19257-19267.
22. X. Du, H. Su and X. Zhang, *ACS Sustainable Chem. Eng.*, 2019, **7**, 16917-16926.
23. B. Beznosikov and K. Aleksandrov, *Crystallogr. Rep.*, 2000, **45**, 792-798.
24. R. D. Shannon, *Acta Crystallogr., Sect. A*, 1976, **32**, 751-767.
25. S. Roy, S. K and U. Rao, *IJMMM*, 2014, **2**, 96-100.
26. S. B. Karki and F. Ramezanipour, *Mater. Today Chem.*, 2019, **13**, 25-33.
27. R. K. Hona, A. Huq, S. Mulmi and F. Ramezanipour, *Inorg. Chem.*, 2017, **56**, 9716-9724.
28. A. Lasia, *INT J HYDROGEN ENERG*, 2019, **44**, 19484-19518.
29. H. Jin, C. Guo, X. Liu, J. Liu, A. Vasileff, Y. Jiao, Y. Zheng and S.-Z. Qiao, *Chem. Rev.*, 2018, **118**, 6337-6408.
30. S. B. Karki and F. Ramezanipour, *ACS Appl. Energy Mater.*, 2020, **3**, 10983-10992.

31. H. Wang, H.-W. Lee, Y. Deng, Z. Lu, P.-C. Hsu, Y. Liu, D. Lin and Y. Cui, *Nat. Commun.*, 2015, **6**, 7261.
32. J. Zheng, Y. Yan and B. Xu, *J. Electrochem. Soc.*, 2015, **162**, F1470-F1481.
33. R. K. Hona, S. B. Karki and F. Ramezanipour, *ACS Sustain. Chem. Eng.*, 2020, **8**, 11549-11557.
34. H. Wang, H. Zhou, W. Zhang and S. Yao, *J. Mater. Sci.*, 2018, **53**, 8951-8962.
35. Q. Gong, Y. Wang, Q. Hu, J. Zhou, R. Feng, P. N. Duchesne, P. Zhang, F. Chen, N. Han, Y. Li, C. Jin, Y. Li and S.-T. Lee, *Nat. Commun*, 2016, **7**, 13216.
36. H. Feng, Z. Xu, L. Ren, C. Liu, J. Zhuang, Z. Hu, X. Xu, J. Chen, J. Wang, W. Hao, Y. Du and S. X. Dou, *ACS Catal.*, 2018, **8**, 4288-4293.
37. Y. H. Li, P. F. Liu, L. F. Pan, H. F. Wang, Z. Z. Yang, L. R. Zheng, P. Hu, H. J. Zhao, L. Gu and H. G. Yang, *Nat. Commun*, 2015, **6**, 8064.
38. X. Xu, Y. Chen, W. Zhou, Z. Zhu, C. Su, M. Liu and Z. Shao, *Adv. Mater.*, 2016, **28**, 6442-6448.
39. Q. Liang, G. Brocks and A. Bieberle-Hütter, *JPhys Energy*, 2021, **3**, 026001.
40. H. Jiang, H. Zhang, Q. Kang, H. Ma, Y. Tong, F. Gao and Q. Lu, *Sci. Rep.*, 2019, **9**, 15681.
41. Y. Zhu, W. Zhou, Z.-G. Chen, Y. Chen, C. Su, M. O. Tadé and Z. Shao, *Angew. Chem. Int. Ed.*, 2015, **54**, 3897-3901.
42. D. Das, A. Das, M. Reghunath and K. K. Nanda, *Green Chem.*, 2017, **19**, 1327-1335.
43. H. W. Park, D. U. Lee, M. G. Park, R. Ahmed, M. H. Seo, L. F. Nazar and Z. Chen, *ChemSusChem*, 2015, **8**, 1058-1065.
44. M. Y. Oh, J. S. Jeon, J. J. Lee, P. Kim and K. S. Nahm, *RSC Adv.*, 2015, **5**, 19190-19198.
45. Y. Zhao, L. Xu, L. Mai, C. Han, Q. An, X. Xu, X. Liu and Q. Zhang, *PNAS*, 2012, **109**, 19569-19574.
46. Y. Zhu, W. Zhou, J. Sunarso, Y. Zhong and Z. Shao, *Adv. Funct. Mater.*, 2016, **26**, 5862-5872.
47. R. K. Hona and F. Ramezanipour, *Angew. Chem.*, 2019, **131**, 2082-2085.
48. T. Saitoh, A. E. Bocquet, T. Mizokawa and A. Fujimori, *Phys. Rev. B*, 1995, **52**, 7934-7938.
49. A. E. Bocquet, T. Mizokawa, T. Saitoh, H. Namatame and A. Fujimori, *Phys. Rev. B*, 1992, **46**, 3771-3784.
50. W. T. Hong, M. Risch, K. A. Stoerzinger, A. Grimaud, J. Suntivich and Y. Shao-Horn, *Energy Environ. Sci.* , 2015, **8**, 1404-1427.
51. J. Suntivich, K. J. May, H. A. Gasteiger, J. B. Goodenough and Y. Shao-Horn, *Science*, 2011, **334**, 1383-1385.
52. Y. Moritomo, K. Higashi, K. Matsuda and A. Nakamura, *Phys. Rev. B* 1997, **55**, R14725-R14728.